Subgrid-Scale Dissipation in the Atmospheric Surface Layer: Effects of Stability and Filter Dimension

FERNANDO PORTÉ-AGEL AND MARC B. PARLANGE

Department of Geography and Environmental Engineering, and Center for Environmental and Applied Fluid Mechanics, The Johns Hopkins University, Baltimore, Maryland

CHARLES MENEVEAU

Department of Mechanical Engineering, and Center for Environmental and Applied Fluid Mechanics, The Johns Hopkins University, Baltimore, Maryland

WILLIAM E. EICHINGER

Iowa Institute for Hydraulic Research, and Department of Civil and Environmental Engineering, University of Iowa, Iowa City, Iowa

MARKUS PAHLOW

Department of Geography and Environmental Engineering, and Center for Environmental and Applied Fluid Mechanics, The Johns Hopkins University, Baltimore, Maryland

(Manuscript received 19 February 1999, in final form 20 June 1999)

ABSTRACT

Field measurements are undertaken with the specific purpose of addressing open issues in subgrid-scale (SGS) modeling of turbulence for large eddy simulation. Wind velocity and temperature signals are obtained using a horizontal linear array of six three-dimensional sonic anemometers placed at a height of 2.15 m in the surface layer over a grass field. From these data, the SGS heat flux and a two-dimensional surrogate of the SGS dissipation of temperature variance (χ) are computed by means of two-dimensional horizontal filtering and by invoking Taylor's hypothesis. Conditional averaging is used to isolate the effects of large-scale structures (sweeps and ejections) of the flow on the SGS dissipation under different stability conditions. During flow events associated with strong increments of vertical velocity (possibly associated with the onset of ejection events), negative values of χ, indicative of transfer of temperature variance from the small scales to the resolved field (backscatter), have an important relative contribution regardless of atmospheric stability. Strong drops in the vertical velocity (possibly associated with the onset of sweeps) are accompanied by large positive values of the SGS dissipation. The two-dimensional SGS dissipation is compared with a one-dimensional surrogate based on a single sensor used in earlier work. The one- and two-dimensional results show qualitatively the same trends. Quantitative differences underscore the advantages of a two-dimensional approach based on the sensor array used in this work.

1. Introduction

Large eddy simulation (LES) has been gaining importance as a tool for the study of momentum and scalar transport in the atmospheric boundary layer (ABL) (Moeng 1984; Nieuwstadt et al. 1991; Shaw and Schumann 1992; Andrén et al. 1994; Sullivan et al. 1994; Parlange et al. 1995; Sorbjan 1996; Dwyer et al. 1997; Avissar and Schmidt 1998; Avissar et al. 1998; Albertson and Parlange 1999a,b).

LES involves solving the filtered three-dimensional unsteady transport equations for momentum and scalar quantities, including temperature and water vapor. A filtering operation, which imposes a separation of scales into resolved scales (larger than the filter width Δ) and subgrid scales (smaller than Δ), is required to allow a numerical solution on a grid with a mesh size of order Δ. The effects of small scales must be parameterized faithfully using a subgrid-scale (SGS) model. Although several SGS models with different degrees of complexity have been used to account for the effects of the nonresolved motions in LES of atmospheric flows, there

Corresponding author address: Fernando Porté-Agel, Dept. of Geography and Environmental Engineering, The Johns Hopkins University, 313 Ames Hall, Baltimore, MD 21218.
E-mail: fporte@jhu.edu

© 2000 American Meteorological Society

is evidence that these models have limitations in capturing all the dynamics of the flow. There currently is no ''universal'' model formulation that does not require some tuning of parameters to match the particular problem being addressed. Current SGS models have trouble reproducing well-established results such as the mean velocity profiles and energy spectra, even in a simple neutrally stratified ABL over a homogeneous surface (e.g., Andrén et al. 1994). ABL simulations are very sensitive to the type of SGS model used and to the value of the model parameters. This case is particularly true in the near-surface region, where the contribution of the nonresolved scales is the largest. For an extensive review of SGS models used for LES of atmospheric flows, see Mason (1994). To capture the effects of the nonresolved motion, improved formulations of the SGS models are needed, particularly if the simulations are intended to be a tool to improve understanding of the transport processes that occur at the land–atmosphere interface. The current paper employs special field measurements to address important issues in SGS modeling of the ABL and continues work initiated by Porté-Agel et al. (1998). The use of field measurements to address LES modeling questions also has been proposed recently in Tong et al. (1998).

If the convection–diffusion equation that describes the transport of a scalar quantity θ (e.g., temperature) is filtered spatially, using a filter with a characteristic width Δ, the filtered transport equation

$$\frac{\partial \tilde{\theta}}{\partial t} + \frac{\partial (\tilde{u}_j \tilde{\theta})}{\partial x_j} = -\frac{\partial q_i}{\partial x_i} + \tilde{Q} \tag{1}$$

is obtained, where t is time, x_j is the spatial coordinate in the j direction, u_j is the velocity component in the j direction, and Q is a source term. The molecular diffusion has been neglected, and the tilde ($\sim$) denotes the filtering operation. The vector component q_i is the SGS scalar flux in the i direction, defined as

$$q_i = \widetilde{u_i \theta} - \tilde{u}_i \tilde{\theta}. \tag{2}$$

This term describes the effects of the unresolved scales (smaller than Δ) on the evolution of $\tilde{\theta}$, and it must be parameterized as a function of the resolved field. Similar expressions hold for the momentum transport, but here scalar transport is focused on.

The subgrid scales can affect strongly the level of fluctuations in the resolved scalar field. A measure of this variability is the filtered scalar variance $\sigma_\theta^2 = \langle \frac{1}{2} \tilde{\theta}'^2 \rangle = \frac{1}{2} \langle (\tilde{\theta} - \langle \tilde{\theta} \rangle)^2 \rangle$, where $\langle\ \rangle$ denotes the ensemble average and the prime is the departure from that average: $\tilde{\theta} = \langle \tilde{\theta} \rangle + \tilde{\theta}'$. In the absence of sources and neglecting molecular effects on the resolved scales, the equation describing the dynamics of σ_θ^2 is

$$\frac{\partial \sigma_\theta^2}{\partial t} + \frac{\partial (\langle \tilde{u}_j \rangle \sigma_\theta^2)}{\partial x_j} = -\frac{\partial}{\partial x_j} \left(\left\langle \tilde{u}_j' \frac{1}{2} \tilde{\theta}'^2 \right\rangle + \langle q_i \tilde{\theta}' \rangle \right) - \langle \tilde{u}_j' \tilde{\theta}' \rangle \frac{\partial \langle \tilde{\theta} \rangle}{\partial x_j} - \langle \chi \rangle, \tag{3}$$

where the first two terms on the right-hand side of Eq. (3) represent spatial transport from resolved and unresolved motion, respectively; the third term is production of resolved temperature fluctuations caused by mean gradients; and the last term is the ensemble average of

$$\chi = -q_j \frac{\partial \tilde{\theta}'}{\partial x_j}. \tag{4}$$

In Eq. (4), χ is the so-called SGS dissipation rate of scalar variance. It also is equal to the production of unresolved temperature fluctuations. Porté-Agel et al. (1998) present the detailed derivation of Eq. (3). The SGS dissipation has a dominant effect on the evolution of σ_θ^2. Since on average one expects a net drain of resolved scalar variance into the subgrid scales, one typically observes $\langle \chi \rangle$ greater than 0.

To make fundamental progress on SGS model development, understanding of the nature of the important quantities that the model describes (such as the SGS dissipation of resolved variance) and how they relate to the large-scale features of the flow needs to be improved. Such understanding can be facilitated with the use of empirical information, that is, field data. The so-called a priori studies use well-resolved turbulent fields, from which the SGS fluxes and SGS dissipation of scalar variance can be computed according to their definition [see Eqs. (2) and (4)]. This approach first was used with data from direct numerical simulations in isotropic turbulence (e.g., Clark et al. 1979; Domaradski et al. 1993) and then was applied to other turbulent flows (e.g., Piomelli et al. 1988; Härtel and Kleiser 1993) and laboratory data (Meneveau 1994; Liu et al. 1994). Such analysis later was expanded to include conditional averaging techniques (Piomelli et al. 1996; O'Neil and Meneveau 1997).

Recently, Porté-Agel et al. (1998) carried out an a priori study of the basic characteristics of the SGS heat fluxes and dissipation of temperature variance in the atmospheric surface layer. They used high-frequency wind velocity and temperature data sampled with a three-dimensional sonic anemometer at a point (at a height of 1.7 m) in the surface layer. The SGS heat fluxes and SGS dissipation were computed according to their definition [Eqs. (2) and (4)]. Porté-Agel et al. (1998) identified the presence of negative values of the streamwise contribution to the SGS dissipation that were associated with backscatter of temperature variance, that is, transfer of temperature variance from the small scales to the resolved field. They also noted the failure of the traditional eddy diffusivity SGS model to reproduce the negative SGS dissipation, since the model is fully dissipative by construction.

A particularly desirable feature of an SGS model is the ability to reproduce the SGS dynamics associated with (and responsible for) large-scale structures of the flow such as coherent structures. Coherent structures in wall-bounded turbulent flows consist of upward motions

of fluid (ejections) alternating with downward motions (sweeps). When there is a vertical temperature gradient forced by the cooling or heating of the surface (stable and unstable conditions in the atmospheric surface layer, respectively), these structures can be identified clearly by looking at the temperature signals. For example, signals measured at a single point typically present ''ramps,'' that is, well-defined sawtooth shaped patterns that occur repeatedly (e.g., Gao et al. 1989; Shaw et al. 1983, 1989; Gao and Shaw 1992; Raupach et al. 1991; Katul et al. 1997b; Szilagyi et al. 1999). Under diurnal convective (buoyant) conditions over a relatively hot and wet surface, the coherent structures of the flow are composed of ejection motions transporting warm and moist air upward, alternating with sweeps of cool and dry air from aloft. These coherent structures have been shown to be responsible for a very important fraction 75% and more) of the total turbulent fluxes (e.g., Gao et al. 1989). Porté-Agel et al. (1998) used conditional averaging to isolate the effects of the large structures of the flow on the SGS dynamics. They showed that coherent structures largely explained the SGS flux and dissipation of the temperature variance. Particularly, they found that strong increases in the resolved temperature (possibly associated with the onset of ejection regions of warm air) under unstable convective conditions are associated with negatives values of the streamwise contribution to the SGS dissipation of the temperature variance.

The study of Porté-Agel et al. (1998) had two limitations. The first relates to instrumentation; only one probe was used. This limitation allowed only one-dimensional filtering to be combined with Taylor's hypothesis. A one-dimensional (streamwise) surrogate of the SGS dissipation of temperature variance was computed, since only derivatives in the streamwise direction could be evaluated (using Taylor's hypothesis). Second, only unstable atmospheric conditions were considered in that study.

In this work, the limitations of the previous study are addressed. First, the a priori analysis of the SGS dissipation of the temperature variance in the atmospheric surface layer is extended to a two-dimensional approach. This extension is done by using data from six three-dimensional sonic anemometers placed in a horizontal array that is nearly perpendicular to the main wind direction. A two-dimensional (horizontal plane) spatial distribution of the wind velocity components and the temperature is obtained by using Taylor's hypothesis on the data sampled with the six anemometers. A two-dimensional filter is used to obtain the SGS heat fluxes as defined by Eq. (2). Moreover, the fact that derivatives of the filtered temperature signal can be evaluated in two directions (streamwise and spanwise) allows two components of the SGS dissipation of temperature variance to be obtained according to Eq. (4). A two-dimensional surrogate of the SGS dissipation of temperature variance also is obtained by the addition of the streamwise and spanwise components.

The second objective of this study is to investigate the influence of atmospheric stability on the dynamics of the subgrid-scale variables. For both stable and unstable conditions, we try to isolate the influence of large-scale structures of the flow on the magnitude of the subgrid-scale dissipation of the resolved temperature variance by using conditional averaging.

2. Experiment

The atmospheric surface layer data used in this study were obtained in a field experiment carried out in Amana, Iowa, during the summer of 1998. The site was a flat field (some 800 m $\times$ 600 m) with grass cover. The data were taken near the center of the field to guarantee a long fetch (more than 400 m) with homogeneous, flat terrain in the upwind direction.

Six Campbell Scientific, Inc., CSAT3 triaxial sonic anemometers (path length = 10 cm) were used to measure simultaneously the longitudinal (u_1), lateral (u_2), and vertical (u_3) wind velocity components and the air temperature (θ). Four of the anemometers sampled at 60 Hz, one of them at 40 Hz, and the other at 20 Hz. The supporting meteorological measurements included net radiation, water vapor concentration, relative humidity, and surface temperature.

Analysis of data from two 15-min periods, from 1110 to 1125 LST (period *U*) and from 1225 to 1240 LST (period *S*) on 3 July 1998 is presented. LST lags UTC by 6 h. The sonic anemometers were placed in a horizontal array nearly perpendicular to the prevailing wind and at a height z of 2.15 m. The sensors were equally spaced, each 0.51 m (d) apart from the adjacent sensors. Figures 1a,b show a sketch of the relative position of the anemometers. The angle between the direction of the mean wind and the direction perpendicular to the sensors β was 20.0° for period *U* and $-24.5°$ for period *S.* The reference system is chosen so that i equal to 1, 2, and 3 correspond to the streamwise, spanwise, and vertical directions, respectively.

Since the spanwise direction (perpendicular to the direction of the mean wind for each period) does not correspond exactly with the direction of alignment of the sensors, a shift is applied to the time series based on the use of Taylor's frozen flow hypothesis in order to have simultaneous readings in the positions that correspond to the y axis (dashed line in Fig. 1a). Therefore, the distance between two adjacent sensors in the y direction is $\delta = d\cos\beta$, which in this case corresponds to 0.48 and 0.46 m for periods *U* and *S,* respectively. Also, at this point the signal corresponding to the sensors that sample at 40 and 60 Hz are filtered to 10 Hz and resampled at 20 Hz to allow for simultaneous values of the variables at all six transverse positions. The average grass height was 20 cm and the momentum roughness length z_0 was 0.026 m. Table 1 has a summary of

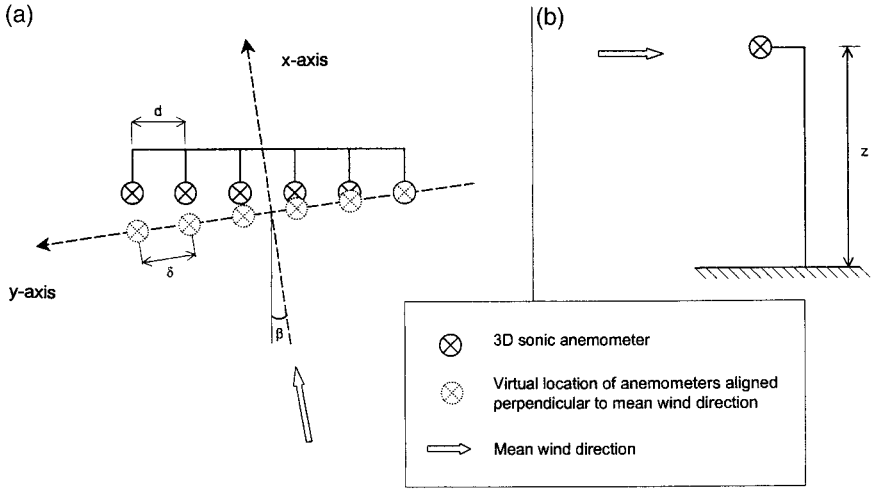

FIG. 1. Sketch of the instrument setup. (a) Plan view; (b) lateral view (parallel to the *y* axis).

the mean meteorological and turbulence conditions for both measurement periods. No large change in these conditions was observed throughout each measurement period. From Table 1, the stability parameter z/L was -0.0275 for period *U* and $+0.0189$ for period *S*, indicating unstable and stable atmospheric stability conditions, respectively. Here L is the Obukhov length,

$$L = \frac{-u_*^3}{\kappa g H/(\rho C_p T)}, \tag{5}$$

where $u_* = (\tau/\rho)^{1/2} = (-\langle u_1' u_3' \rangle)^{1/2}$ is the friction velocity, τ is the surface shear stress, ρ is the density of air, H is the sensible heat flux, C_p is the heat capacity, T is the mean air temperature, g is the gravitational acceleration, and κ (=0.4) is von Kármán's constant. Period *S* was stable because of the arrival of extensive cloud cover. A number of other periods corresponding to unstable and stable atmospheric conditions were analyzed, including nocturnal datasets. For brevity in this paper, results from only two periods are presented. The results from the periods used in the analysis are typical for what was found in the complete dataset. They were selected because many important variables, such as grass height (i.e., surface roughness), mean wind velocity, and wind direction, are very similar for both periods. This similarity allows the effect of atmospheric stability on the SGS quantities to be isolated.

TABLE 1. Summary of meteorological and turbulence conditions during the experiment.

Meteorological and turbulence conditions	Period *U*	Period *S*
Mean horizontal wind speed ($\langle u_1 \rangle$)	3.15 m s^{-1}	4.26 m s^{-1}
Mean air temperature ($\langle \theta \rangle$)	302.42 K	301.65 K
rms horizontal velocity (σ_{u_1})	0.77 m s^{-1}	1.28 m s^{-1}
rms vertical velocity (σ_{u_3})	0.35 m s^{-1}	0.44 m s^{-1}
rms temperature (σ_θ)	0.21 K	0.50 K
Friction velocity (u_*)	0.30 m s^{-1}	0.38 m s^{-1}
Streamwise heat flux ($\langle u_1 \theta' \rangle$)	-0.0920 K m s^{-1}	$+0.049$ K m s^{-1}
Vertical heat flux ($\langle u_3' \theta' \rangle$)	$+0.026$ K m s^{-1}	-0.037 K m s^{-1}
Obukhov length (L)	-78.3 m	$+114.0$ m
Stability parameter (z/L)	-0.0275	$+0.0189$

The power spectra for the streamwise velocity and temperature signals from the measurement periods *U* and *S* are computed and presented in Figs. 2a and 2b, respectively. They are obtained from 25 segments of 1024 points each, using a Bartlett window (Press et al. 1992). In Fig. 2, the power spectra (E_k for a generic signal k) are normalized as $E_k/(\sigma_k^2 z)$, where σ_k^2 is the variance of the signal. The wavenumber k_1 is based on the sampling frequency, using Taylor's hypothesis, and is normalized by z. The slope of the spectrum is $-5/3$ for a wide range of wavenumbers, indicative of the inertial subrange. At smaller wavenumbers, the slope is lower. The fact that the spectrum for the temperature signal has a steeper slope in the smallest wavenumbers is indicative of a trend in the mean temperature. Since this trend has no effect on the subgrid-scale quantities computed and presented in section 3, no effort was made to detrend the data.

3. Data analysis and results

a. SGS heat fluxes and surrogates of the dissipation of temperature variance

Each component of the SGS heat flux q_i is computed according to its definition [Eq. (2)]. Because of the limitations imposed by the number of sensors and the arrangement used, three-dimensional filtering is not possible. Instead, a two-dimensional filter is used, which consists of the combination of a Gaussian filter in the streamwise direction and a box filter in the direction parallel to the sensors.

For a generic variable $\alpha(x, y)$, where x and y are the streamwise (x_1) and spanwise (x_2) spatial coordinates, respectively, the filtered variable $\tilde{\alpha}(x, y_J)$, corresponding

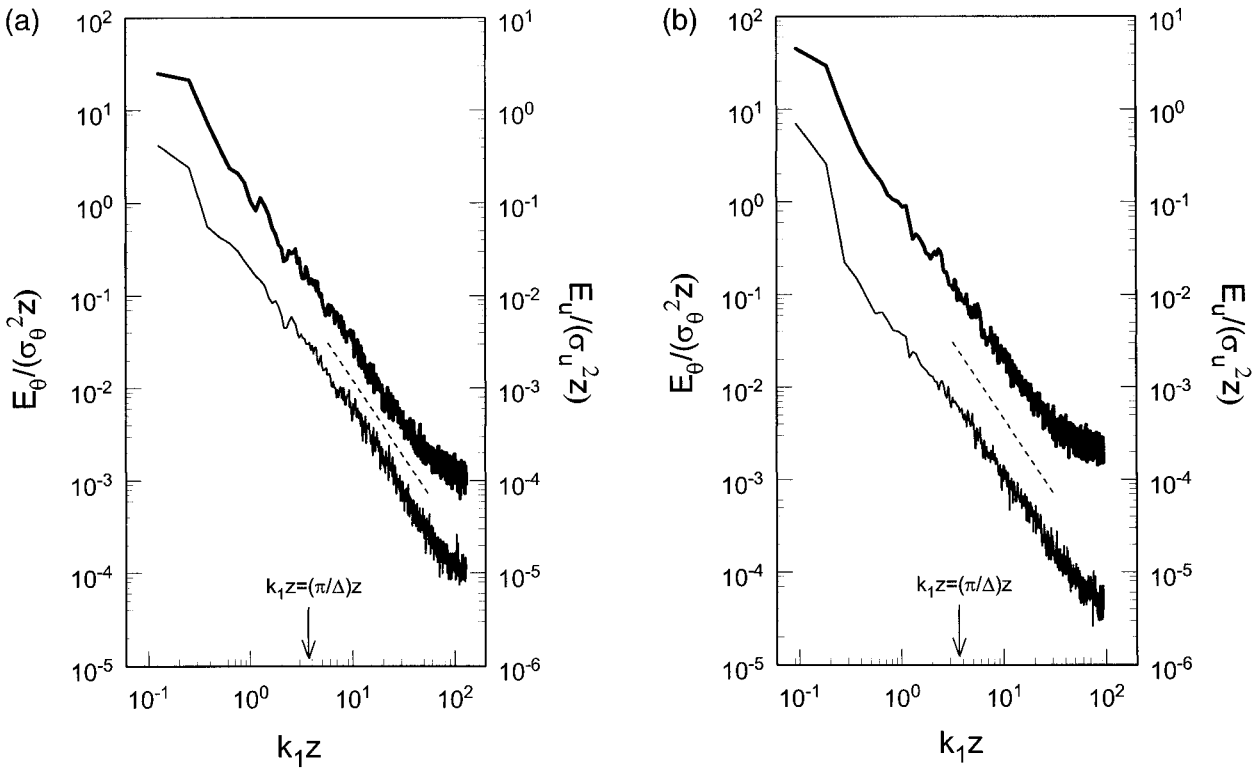

FIG. 2. Normalized power spectra for the streamwise velocity (thick line) and the temperature (light line) for (a) measurement period *U* and (b) period *S*. The −5/3 power law is also shown (dashed line). The arrows show $k_1 z$ corresponding to the filter scale Δ (see section 3a).

to the lateral position y_J, is computed as follows. A box filter is applied in the spanwise direction and consists of the average $\overline{\alpha}(x, y_J) = (1/N)\ \Sigma\ \alpha(x, y_j)$, where y_j is the lateral position of each of the N sensors centered around the ordinate y_J. The number N was chosen to be 4 (instead of 6) to allow computation of the derivative of the filtered temperature using centered finite differences, as shown below. This choice yields a filter size $\Delta = N\delta = 1.92$ m and 1.84 m for periods *U* and *S*, respectively. The average $\overline{\alpha}(x, y_J)$ then is filtered in the streamwise direction by convolution with a filter function G_Δ:

$$\tilde{\alpha}(x, y_J) = \int \overline{\alpha}(x, y_J) G_\Delta(x - x')\, dx',$$

where x' is an integration variable. For computational convenience, the filtering is done in wave space using the fast Fourier transform (Press et al. 1992). The results presented here were obtained using a Gaussian filter whose Fourier transform is of the form $\hat{G}_\Delta = \exp[-(k_1^2\Delta^2)/24]$, where k_1 is the wavenumber and Δ is the filter size. The filter size was chosen to be $N\delta$, equal to the filter size in the transverse direction. As shown in Fig. 2, the selected filter size (wavenumber $k_1 = \pi/\Delta$) falls near the upper limit of the inertial subrange, characterized by the −5/3 slope in the spectra. Three other filter types, box filter, spectral cutoff, and top hat, also were tested in the streamwise direction and similar results were obtained. This result is in agreement with previous research (e.g., Meneveau 1994), which found that the impact of using different filter types on the SGS flux, SGS dissipation, model coefficients, etc., typically is small.

Taylor's hypothesis in the inertial subrange often is applied in the atmospheric surface layer with turbulent intensities (root-mean-square to mean longitudinal velocity ratio) of up to 30% and more (e.g., Peltier et al. 1996; Kiely et al. 1996; Katul et al. 1997a), and it was justified by Wyngaard and Clifford (1977). Recently, Tong et al. (1998) used data from an LES of the ABL to study the validity of Taylor's hypothesis for approximating streamwise filtering with time filtering. They concluded that, although the fluctuations in the convection velocity have some effect on the computed SGS fluxes and stresses because of the change in the effective filter size and shape, the sensor array is a feasible technique for SGS measurement in the atmospheric surface layer.

A segment of the streamwise (q_1), spanwise (q_2), and vertical (q_3) SGS heat fluxes is presented in Fig. 3, corresponding to a fraction of the measurement period *U*. Clearly the spatial distribution of this variable is intermittent. Figure 4 shows the probability density functions (pdf) of q_1, q_2, and q_3, normalized with their standard deviation. The SGS heat fluxes show a clear

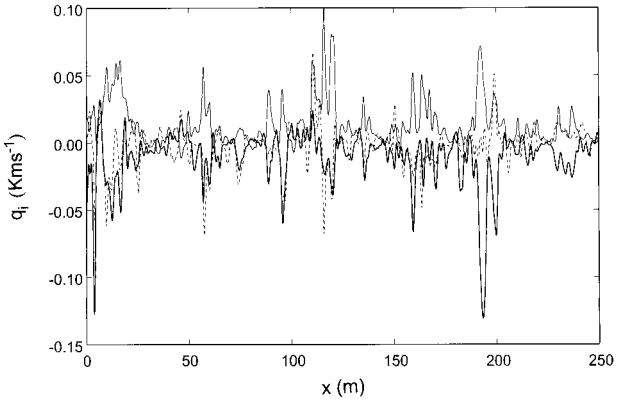

FIG. 3. Portion of the three components of the SGS heat flux signals: streamwise q_1 (thick solid line), spanwise q_2 (thin solid line), and vertical q_3 (dashed line). They are evaluated from data obtained with an array of sonic anemometers, using 2D filtering.

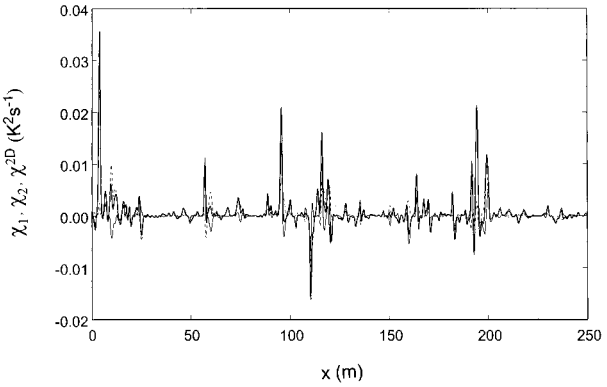

FIG. 5. Portion of the surrogates of the two components of the SGS dissipation of the temperature variance: streamwise χ_1 (thin solid line), spanwise χ_2 (dashed line), and 2D surrogate $\chi^{2D} = \chi_1 + \chi_2$ (thick solid line).

non-Gaussian behavior, with a strong asymmetry in the pdfs of q_1 and q_3, and exponential tails.

Two components (out of three) of the SGS dissipation of temperature variance, χ_1 and χ_2, corresponding to the streamwise and spanwise directions, respectively, are computed according to their definition [Eq. (4)] but with no summation over *j*. Derivatives of the filtered temperature are evaluated using centered differences over a distance corresponding to the data acquisition rate (32 cm). In the *y* direction, the derivative involves the difference between the filtered values at y_J equal to $\pm\delta$. A two-dimensional surrogate of the SGS dissipation of temperature variance χ^{2D} also is obtained by adding the two components ($\chi^{2D} = \chi_1 + \chi_2$). In Fig. 5 segments of the two components of the SGS dissipation as well as the 2D surrogate are presented, corresponding to a fraction of period *U*. The signals have a very strong degree of intermittency and all three of them have negative values, indicating backscatter, that is, transfer of temperature variance from the small scales to the large scales. These qualitative observations are similar to the one-dimensional results obtained by Porté-Agel et al. (1998). The pdfs of χ_1, χ_2, and χ^{2D}, shown in Fig. 6, also are very different from the Gaussian distribution. The strong asymmetry shows that the positive average value of χ (forward cascade of scalar variance in the mean) is due to a few very strong positive events that occur more frequently than strong negative events. Such a behavior also was observed for kinetic energy dissipation using the wavelet decomposition (Meneveau 1991).

b. Conditional average of the SGS heat fluxes and dissipation of temperature variance

In Fig. 7, two-dimensional color contour plots of the streamwise velocity u_1, vertical velocity u_3, and tem-

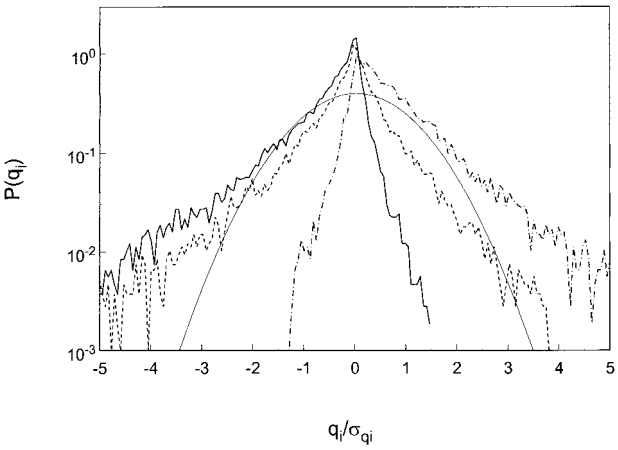

FIG. 4. Probability density function of the three components of the SGS heat flux, normalized with their standard deviations: streamwise q_1 (solid line), spanwise q_2 (dashed line), and vertical q_3 (dotted–dashed line). The thin solid line is the Gaussian distribution with zero mean.

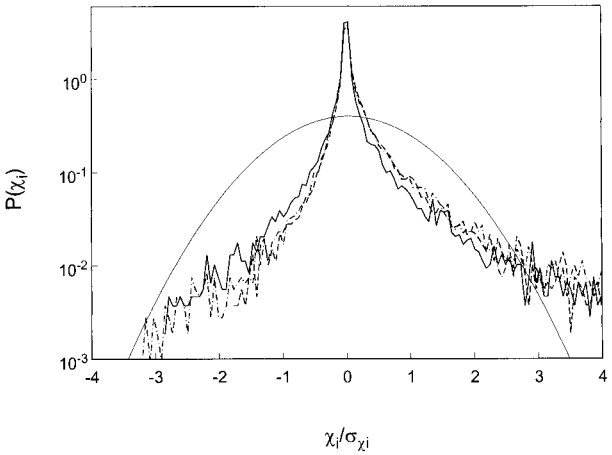

FIG. 6. Probability density function of the surrogates of the SGS dissipation of the temperature variance: streamwise χ_1 (solid line), spanwise χ_2 (dotted–dashed line), and 2D surrogate $\chi^{2D} = \chi_1 + \chi_2$ (dashed line). The thin solid line is the Gaussian distribution with zero mean.

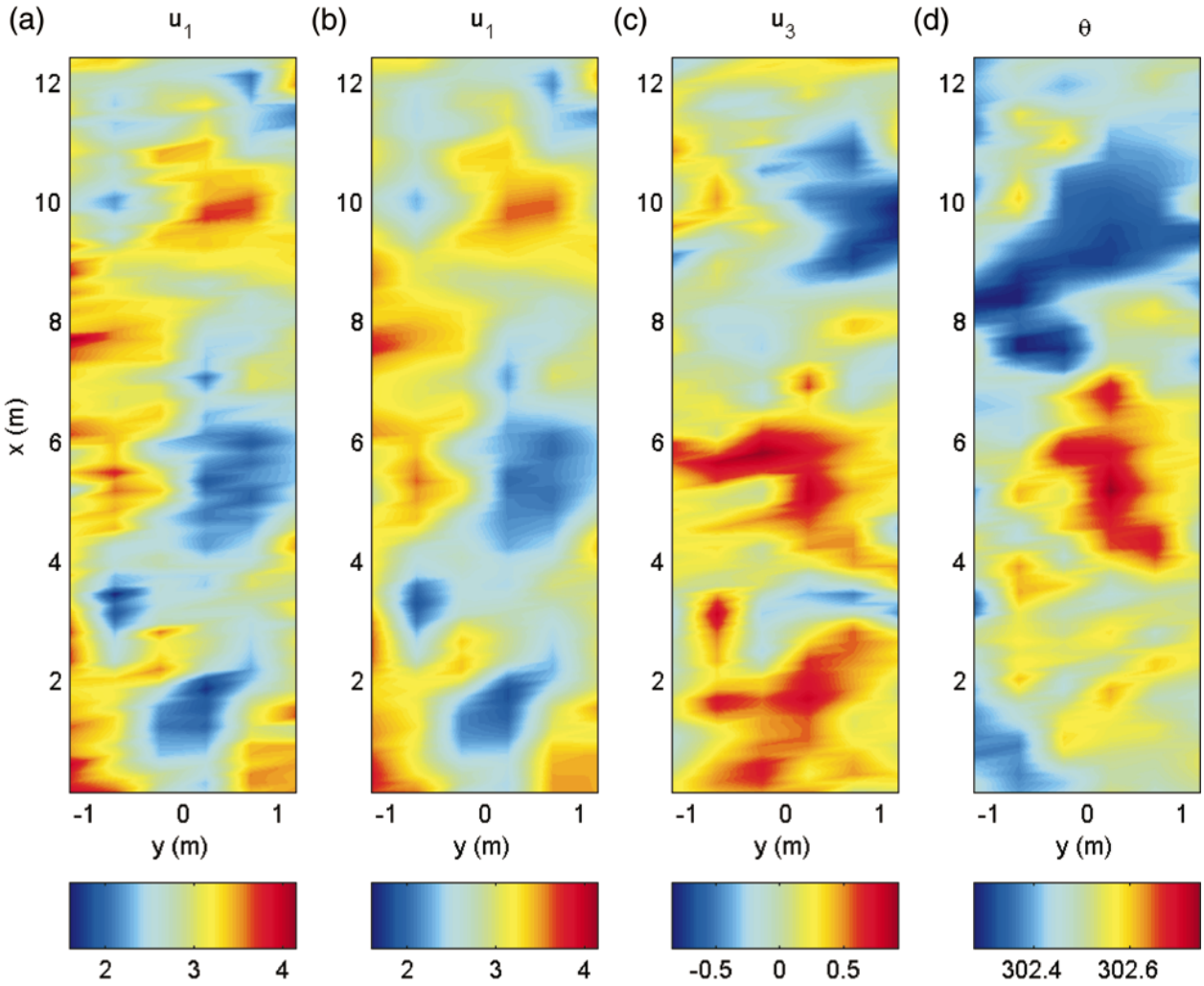

FIG. 7. Contour plot of (a), (b) the streamwise velocity (u_1; m s^{-1}); (c) vertical velocity (u_3; m s^{-1}); and (d) temperature (θ; K) corresponding to period U. For presentation purposes, a box filter of size δ is used in the streamwise direction in (b), (c), and (d).

perature θ are shown, corresponding to the measurement period U. The short axis corresponds to the direction perpendicular to the main wind, or nearly parallel to the sensors (y direction). The longer axis corresponds to the direction of the main wind (x direction) and is obtained using Taylor's frozen flow hypothesis to convert the time coordinate into a space coordinate. Figure 7a presents the raw values of u_1. It shows a clear difference in resolution in the two directions because of the high frequency at which measurements were taken compared with the resolution in the spanwise direction imposed by the number of sensors (six) used. Only for presentation purposes, the signals are filtered in the streamwise direction using a box filter of size equal to δ and are presented in Figs. 7b–d.

In Fig. 7 the presence of structures of the flow can be identified as can be their relative size and horizontal dimensions. Note that their relative size is comparable with and smaller than Δ, which means that they have an important influence on the dynamics of the SGS variables. There is clear evidence of the well-established result of negative correlation between the streamwise and vertical velocity fluctuations ($\langle u_1' u_3' \rangle < 0$) in wall-bounded turbulent flows. A deceleration of the flow in the streamwise direction ($u_1' < 0$) is associated with an upward motion or ejection of the air ($u_3' > 0$) from below. Under unstable conditions, as in period U, these ejections carry relatively warm air upward, producing an increase in the temperature ($\theta' > 0$).

To isolate the effect of coherent structures of the flow (sweeps and ejections) on the subgrid-scale dynamics, conditional averaging is performed on the SGS heat fluxes and dissipation of the temperature variance in the same fashion as presented in Porté-Agel et al. (1998). The conditional average of a generic SGS variable $\Phi(x, y_J)$ under the condition C in a window of size W is defined according to

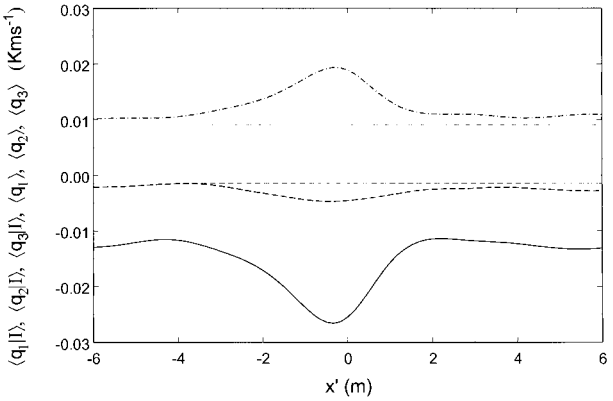

FIG. 8. Conditionally averaged SGS heat flux, under condition I ($\partial\theta/\partial t < -\sigma_{\partial\theta/\partial t}$), for measurement period *U* (unstable surface layer). Streamwise component $\langle q_1 | \mathrm{I}\rangle$ (solid line), spanwise component $\langle q_2 | \mathrm{I}\rangle$ (dashed line), and vertical component $\langle q_3 | \mathrm{I}\rangle$ (dotted–dashed line). Light lines correspond to the overall means.

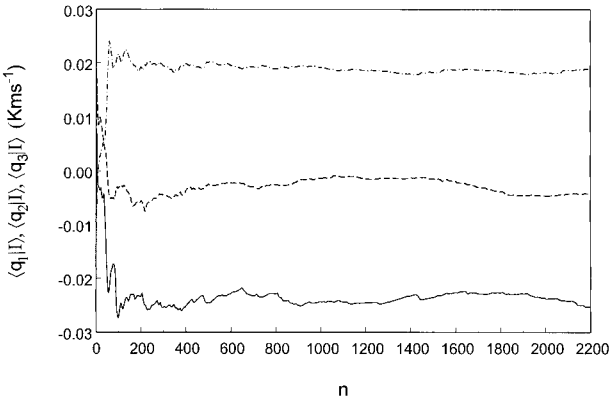

FIG. 9. Running conditional averages of the SGS fluxes at $x' = 0$, under condition I ($\partial\theta/\partial t < -\sigma_{\partial\theta/\partial t}$), for measurement period *U*, as a function of the number of points *n* used for the averaging. Streamwise $\langle q_1 | \mathrm{I}\rangle$ (solid line), spanwise $\langle q_2 | \mathrm{I}\rangle$ (dashed line), and vertical $\langle q_3 | \mathrm{I}\rangle$ (dotted–dashed line).

$$\langle \Phi \,|\, C\rangle(x', y_J) = \frac{1}{n}\sum_{i=1}^{n} \Phi(x_i + x', y_J)$$

$$-\frac{W}{2} \le x' \le +\frac{W}{2}, \qquad (6)$$

where x_i (with $1 \le i \le n$) are the points where $\Phi(x_i, y_J)$ satisfies the condition *C*. For a point located at a position x' in the averaging window, the conditional average $\langle \Phi \,|\, C\rangle$ is computed by averaging all Φ values at points that are located at a distance x' from the points that satisfy the condition (upstream if $x' < 0$ and downstream if $x' > 0$). For instance, for $x' = 0$ (center of the averaging window), the value of the conditional average is computed from the values of Φ at points that satisfy the condition.

Conditional averaging was applied to the SGS heat fluxes (q_1, q_2, and q_3) and the surrogates of the SGS dissipation (χ_1, χ_2, and χ^{2D}). To isolate the different parts of the temperature fields, which may be indicative of different regions within coherent structures of the flow, the conditions used are based on the gradient of the resolved temperature $\partial\tilde{\theta}/\partial t$. Two conditions are used.

1) Condition I: $\partial\tilde{\theta}/\partial t < -\sigma_{\partial\tilde{\theta}/\partial t}$, where $\sigma_{\partial\tilde{\theta}/\partial t}$ is the root-mean-square of $\partial\tilde{\theta}/\partial t$. This condition corresponds to a temperature drop in the time series and tends to highlight the decreasing part of possible ramp structures.
2) Condition II: $\partial\tilde{\theta}/\partial t > \sigma_{\partial\tilde{\theta}/\partial t}$ corresponds to a temperature increase in the time series. This condition highlights the rising part of the temperature signal.

The selection of the conditioning threshold $\sigma_{\partial\tilde{\theta}/\partial t}$ is arbitrary and is chosen simply to guarantee that it is large enough to isolate the local effects and small enough to ensure the convergence of conditional averages. The width of the averaging window *W* was set to 6.5 times the filter width, that is, *W* equals 12.5 m. As in Porté-Agel et al. (1998), the value of *W* has no effect on the average but allows the entire portion of interest around x' equal to 0 to be shown. The conditional average then moves asymptotically to the overall average as one moves away from the center of the averaging window (at $x' = 0$). The number of points satisfying each condition was high enough to guarantee a good convergence of the conditional averages.

The conditional averages for q_1, q_2, and q_3 under condition I, as well as the overall averages, are presented in Fig. 8, corresponding to the measurement period *U*. The overall averages are $\langle q_1\rangle = -0.0106$ K m s^{-1}, $\langle q_2\rangle = -0.0015$ K m s^{-1}, and $\langle q_3\rangle = 0.0090$ K m s^{-1}. Note that q_1 and q_3 represent 12% and 35% of the total turbulent heat fluxes, respectively (see Table 1). Relatively strong drops (in time) of the temperature are associated with SGS fluxes that are larger in magnitude (more than two times larger) than the average. The good convergence of the conditional averages for the SGS heat fluxes is illustrated in Fig. 9, where the conditional averages at the center point of the averaging window ($x' = 0$) are plotted against the number of points *n* that are used to compute the conditional average, according to Eq. (6).

The conditional averages for χ_1, χ_2, and χ^{2D} under condition I, as well as the overall averages, are presented in Fig. 10, corresponding to the measurement period *U*. The overall averages are $\langle \chi_1\rangle = 2.50 \times 10^{-4}$ K^2 s^{-1}, $\langle \chi_2\rangle = 3.20 \times 10^{-4}$ K^2 s^{-1}, and $\langle \chi^{2D}\rangle = 5.70 \times 10^{-4}$ K^2 s^{-1}. A larger than average (about 11 times larger) positive value of the streamwise component of the SGS dissipation χ_1 occurs when there is a strong negative temperature gradient. This large value indicates that under these conditions there is a larger amount of temperature variance being transferred from the large (resolved) to the small (subgrid) scales of the flow. On the other hand, the conditionally averaged spanwise component does not differ substantially from the overall average.

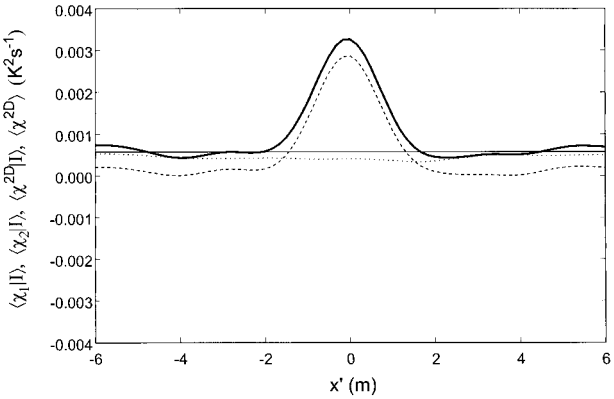

FIG. 10. Conditionally averaged surrogates of the SGS dissipation of temperature variance, under condition I ($\partial\bar{\theta}/\partial t < -\sigma_{\partial\theta/\partial t}$), for measurement period *U* (unstable surface layer). Streamwise component $\langle\chi_1|\mathrm{I}\rangle$ (dashed line), spanwise component $\langle\chi_2|\mathrm{I}\rangle$ (dotted line), and 2D surrogate $\langle\chi^{2D}|\mathrm{I}\rangle$ (thick solid line). The light solid line corresponds to the overall mean 2D surrogate of the SGS dissipation $\langle\chi^{2D}\rangle$.

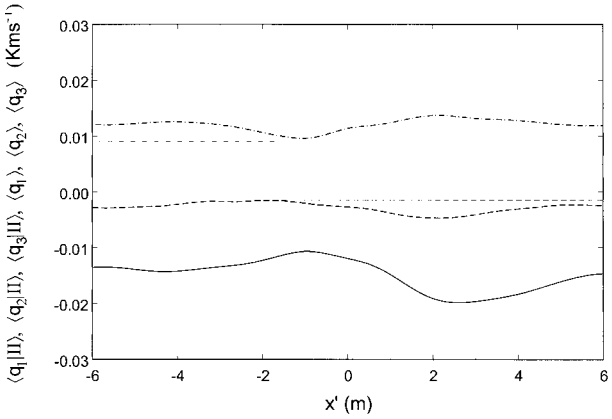

FIG. 11. Conditionally averaged SGS heat flux, under condition II ($\partial\bar{\theta}/\partial t > \sigma_{\partial\theta/\partial t}$), for measurement period *U* (unstable surface layer). Streamwise component $\langle q_1|\mathrm{II}\rangle$ (solid line), spanwise component $\langle q_2|\mathrm{II}\rangle$ (dashed line), and vertical component $\langle q_3|\mathrm{II}\rangle$ (dotted–dashed line). Light lines correspond to the overall means.

The conditional averages for q_1, q_2, and q_3 under condition II are presented in Fig. 11, corresponding to the measurement period *U*. No significant differences with respect to the overall means are observed in this case. In Fig. 12, the conditional averages for χ_1, χ_2, and χ^{2D} under condition 2 are plotted, also corresponding to the measurement period *U*. The conditional average for the streamwise component χ_1 of the SGS dissipation becomes negative and much larger in magnitude than the overall average (about four times larger). The spanwise component χ_2 does not differ substantially from the overall average. The two-dimensional surrogate χ^{2D}, mainly affected by the streamwise component, takes negative values under strong positive temperature gradients (in time) (condition II). It indicates that there is backscatter of temperature variance; that is, temperature variance is being transferred from the subgrid scales of the flow to the resolved field. This result was found also in the 1D analysis carried out by Porté-Agel et al. (1998).

Conditional averaging applied to the resolved vertical velocity (results not presented) shows that strong positive/negative gradients in the filtered temperature typically coincide with strong positive/negative gradients in the resolved vertical velocity. Therefore, backscatter of temperature variance appears to be important during flow events associated with strong increases in resolved vertical velocity. The latter could be indicative of the onset of ejection events.

c. Effects of filter dimensionality

Next, the quantitative differences between the results from the two-dimensional and one-dimensional analyses are documented. As in Porté-Agel et al. (1998), a 1D surrogate dissipation is computed by using the readings of a single anemometer only. It is defined as $\chi_1^{1D} = -q_1(\partial\tilde{\theta}'/\partial x_1)$, where the filtering is performed only in time. Figure 13a shows a comparison of signals of χ_1^{1D} with χ_1. The latter involves also filtering in the cross-stream direction, as described in section 3a. Clearly, there are differences in the details of the signals but also many similarities. The conditional average (using condition 1) of the one- and two-dimensional surrogates of the SGS dissipation (χ^{1D} and χ_1, respectively) are compared in Fig. 13b. Their mean values are very similar, namely, $\langle\chi_1^{1D}\rangle = 2.44 \times 10^{-4}$ K^2 s^{-1} and $\langle\chi_1\rangle = 2.50 \times 10^{-4}$ K^2 s^{-1}. Also, both χ_1^{1D} and χ_1 display the local increase of the conditional average and hence lead to the same qualitative conclusions as in Porté-Agel et al. (1998). However, the conditional average of the 1D surrogate is smaller (about 15% smaller) than the conditional average obtained using the 2D filtering. This quantitative difference between the results, together

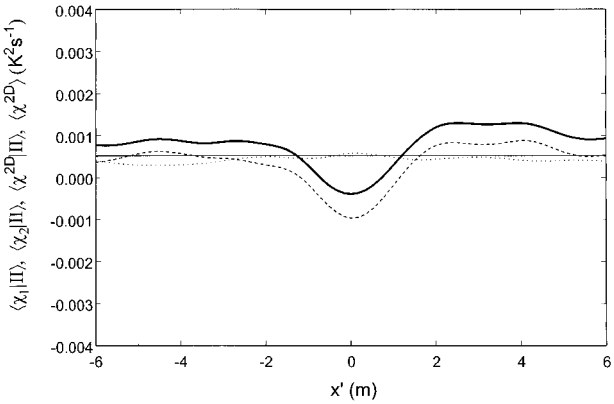

FIG. 12. Conditionally averaged surrogates of the SGS dissipation of temperature variance, under condition II ($\partial\bar{\theta}/\partial t > \sigma_{\partial\theta/\partial t}$), for measurement period *U* (unstable surface layer). Streamwise component $\langle\chi_1|\mathrm{II}\rangle$ (dashed line), spanwise component $\langle\chi_2|\mathrm{II}\rangle$ (dotted line), and 2D surrogate $\langle\chi^{2D}|\mathrm{II}\rangle$ (thick solid line). The light solid line corresponds to the overall mean 2D surrogate of the SGS dissipation $\langle\chi^{2D}\rangle$.

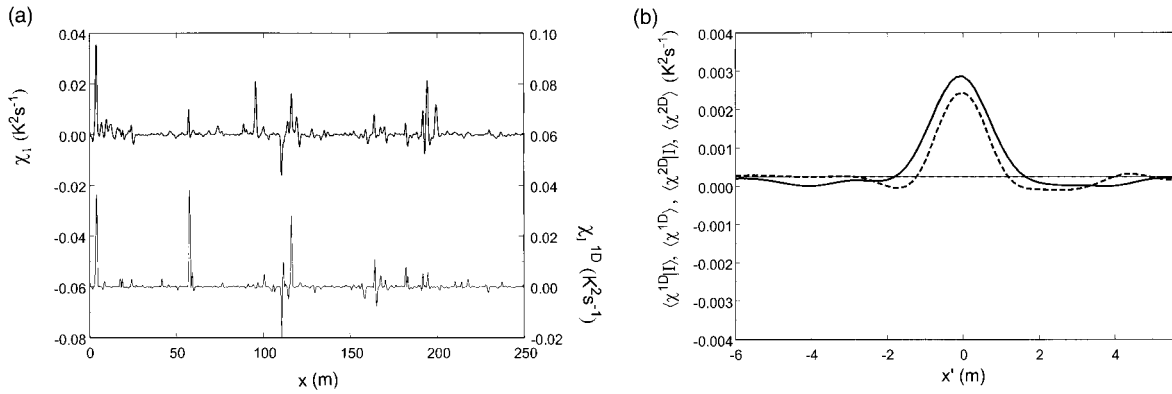

FIG. 13. Comparison between the streamwise SGS dissipation obtained using a 1D filter (χ_1^{1D}) and a 2D filter (χ_1). (a) Portion of signals of χ_1^{1D} (light line) and χ_1 (thick line). (b) Conditional averages under condition I ($\partial\theta/\partial t < -\sigma_{\partial\theta/\partial t}$), for measurement period U: $\langle\chi_1^{1D}|\mathrm{I}\rangle$ (thick dashed line), $\langle\chi_1|\mathrm{I}\rangle$ (thick solid line). Thin lines correspond to the overall means.

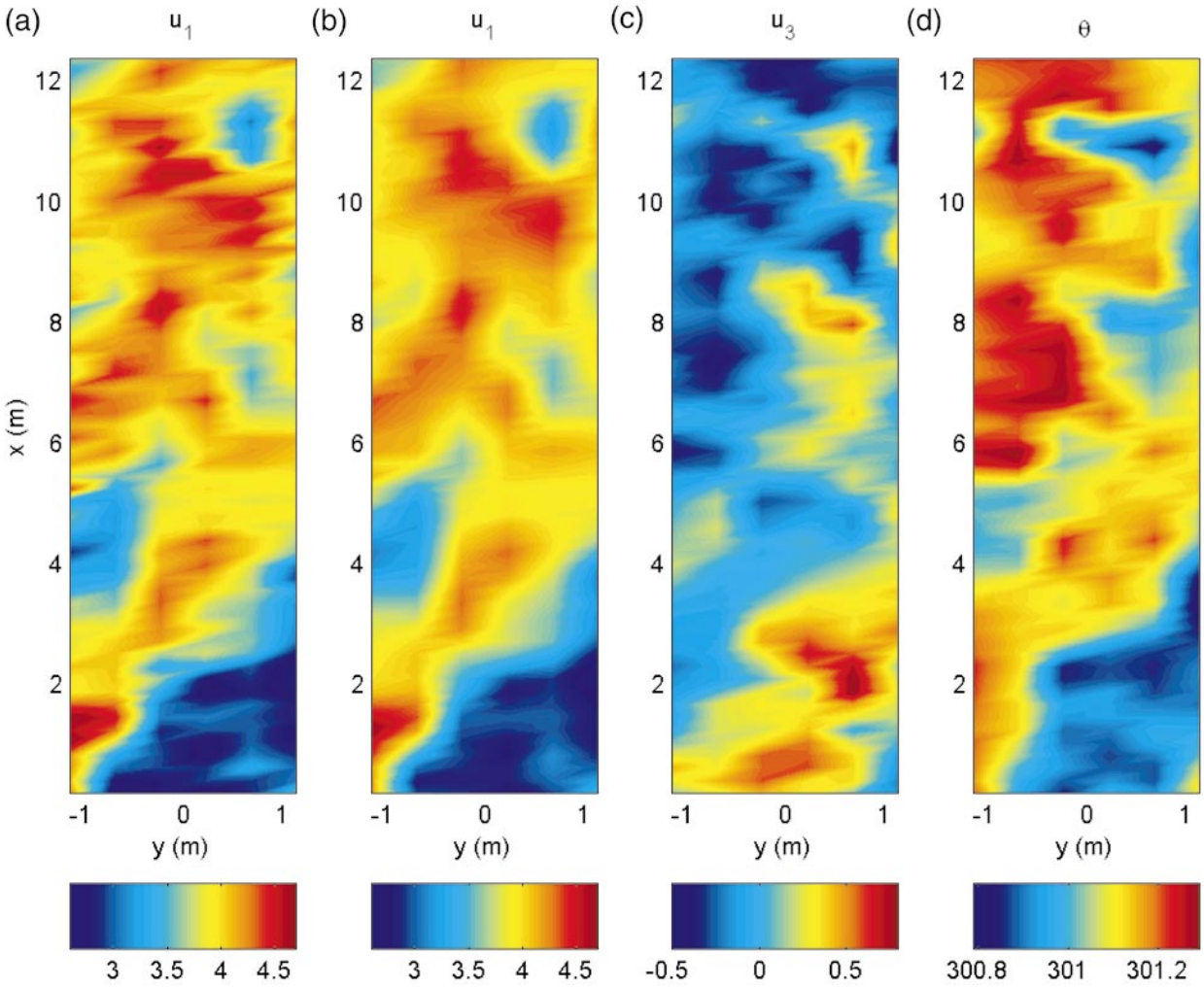

FIG. 14. Contour plot of (a), (b) the streamwise velocity (u_1; m s^{-1}); (c) vertical velocity (u_3; m s^{-1}); and (d) temperature (θ; K) corresponding to period *S*. For presentation purposes, a box filter of size δ is used in the streamwise direction in (b), (c), and (d).

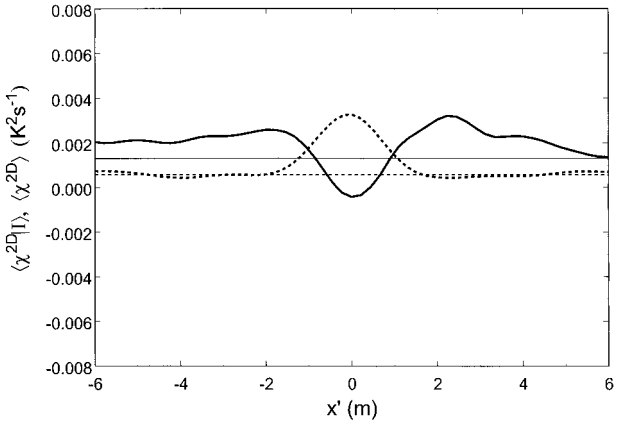

FIG. 15. Conditionally averaged 2D surrogate of the SGS dissipation of temperature variance $\langle \chi^{2D} | \mathrm{I} \rangle$, under condition I ($\partial\bar{\theta}/\partial t < -\sigma_{\partial\bar{\theta}/\partial t}$), for measurement period *U* (unstable; dashed line) and measurement period *S* (stable; solid line). The light lines correspond to the overall mean 2D surrogates of the SGS dissipation.

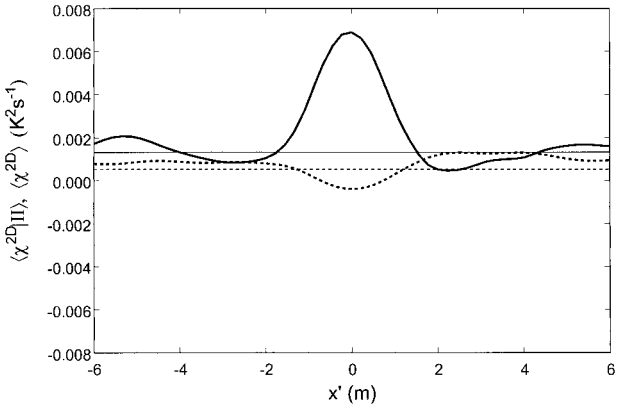

FIG. 16. Conditionally averaged 2D surrogate of the SGS dissipation of temperature variance $\langle \chi^{2D} | \mathrm{II} \rangle$, under condition II ($\partial\bar{\theta}/\partial t > \sigma_{\partial\bar{\theta}/\partial t}$), for measurement period *U* (unstable; dashed line) and measurement period *S* (stable; solid line). The light lines correspond to the overall mean 2D surrogate of the SGS dissipation.

with the fact that the two-dimensional analysis allows χ_2 and thus a two-dimensional surrogate of the dissipation χ_1^{2D} to be computed, justifies the use of a probe array.

d. Influence of atmospheric stability on the conditional average

To study the influence of atmospheric stability on the conditional averages of the SGS dissipation, the conditional analysis (as in section 3b) is carried out on the data obtained during the measurement period *S* under stable conditions.

In Fig. 14, two-dimensional contour plots of the streamwise velocity u_1, vertical velocity u_3, and temperature θ are shown, corresponding to the measurement period *S*. Again, for presentation purposes, the signals are filtered in the streamwise direction using a box filter of size equal to δ. As in Fig. 7, there is evidence of the overall negative correlation between the streamwise and vertical velocity fluctuations ($\langle u_1' u_3' \rangle < 0$). Note that, under stable conditions, ejections ($u_3' > 0$) carry relatively cool air upward, producing a decrease in the temperature ($\theta' < 0$). In a similar way under stable conditions, downward motions or sweeps of air bring relatively warm air from aloft ($\theta' > 0$).

The conditionally averaged two-dimensional surrogate of the SGS dissipation χ^{2D} corresponding to measurement period *S* is presented in Fig. 15 (for condition I) and in Fig. 16 (for condition II) and is compared with the results from the measurement period *U*. The overall average is $\langle \chi^{2D} \rangle = 1.32 \times 10^{-3}$ K^2 s^{-1}. Since at $x' = 0$ the conditional average differs strongly from the overall average, the relative positive (or negative) contribution to the SGS dissipation by flow events associated with large negative (or positive) temperature gradients is very important. Furthermore, there is a clear qualitative change in the direction (sign) of that contribution associated with the change in stability. Under stable conditions, the effect of negative values of the SGS dissipation, associated with backscatter of temperature variance, is high near points of large negative gradients of filtered temperature (condition I). This fact yields a conditionally averaged dissipation that is much lower than the overall average and even slightly negative. Under unstable conditions, negative values of SGS dissipation are associated with positive temperature gradients (condition II). Large positive values (about six times larger than the overall average) are related to positive gradients of temperature (condition II), as opposed to negative gradients (condition I) under unstable conditions.

The different qualitative response of the SGS dissipation signals to conditional averaging under different stability conditions can be understood clearly by considering the change of sign in the correlation between the fluctuations of the vertical velocity and those of the temperature. Under unstable conditions, relatively strong increments in the resolved vertical velocity, highlighted by condition II (strong increases in resolved temperature), are associated with large negative SGS dissipations. Under stable conditions, strong increments of vertical velocity are highlighted mainly by condition I (relatively strong decreases in temperature), and they also are associated with negative SGS dissipations. Therefore, negative values of the SGS dissipation indicative of backscatter have an important relative contribution during flow events associated with strong increments in resolved vertical velocity under both stable and unstable surface layers. This result can be physically understood by recognizing that ejections are associated with bringing small-scale turbulence (which falls below Δ) from close to the ground upward. In contrast, strong drops in vertical velocity are associated with large positive SGS dissipation regardless of stability.

4. Conclusions

A field experiment was carried out to study the basic characteristics of the subgrid-scale heat flux and dissipation of temperature variance in the surface layer and to understand their relation to large-scale structures of the flow under different atmospheric stability conditions. A horizontal array of six three-dimensional sonic anemometers was used to obtain high-resolution two-dimensional spatial distributions of the three components of the wind velocity and temperature, from which SGS heat fluxes and a 2D surrogate of the dissipation of temperature variance were computed using a two-dimensional filter and Taylor's hypothesis.

Conditional averaging was used to relate the magnitude of the SGS quantities to sweep and ejection characteristics of the flow. Under unstable conditions, strong drops in the resolved vertical velocity (and also in the temperature), which possibly correspond with the onset of sweep events, are associated with large positive SGS dissipation of temperature variance. Relatively strong increments in the resolved vertical velocity (and also in temperature), possibly corresponding with the onset of ejection events, are associated with negative dissipation, indicating a transfer of temperature variance from the subgrid (unresolved) scales to the resolved field. The results are in qualitative agreement with the one-dimensional analysis carried out by Porté-Agel et al. (1998).

Despite the change in the vertical mean temperature gradient under stable conditions, strong drops in the resolved vertical velocity (now corresponding to temperature increases) still are associated with large positive SGS dissipations of temperature variance. Also, under stable conditions, negative SGS dissipations indicative of backscatter have an important relative contribution during strong increments in the resolved vertical velocity (now associated with temperature drops).

A priori tests by Piomelli et al. (1996) based on filtered direct numerical simulations of channel flow indicated that backscatter of resolved kinetic energy tends to occur during sweeps, and positive SGS dissipation is associated with ejection events. In a very recent paper, Lin (1999) reexamines this issue based on analysis of resolved kinetic energy dissipation from LES with an eddy-viscosity model. He concludes that, during ejections, both forward scatter and backscatter occur, and the same is true during sweep events. In the current work, the conditioning is based on the temporal gradient of the resolved temperature, which we believe tends to highlight the onset of ejections (with strong increases in temperature and vertical velocity under unstable conditions) or the onset of sweeps (with strong drops in temperature and vertical velocity), as opposed to the entire ejection or sweep region. Further measurements, such as using vertical arrays of sensors to capture the vertical distribtion of the coherent structures, are needed to clarify further the relationship between the current findings and those of Lin (1999) and Piomelli et al. (1996).

Given the important contribution of coherent structures of the flow to the total and SGS fluxes, it is of great significance that the subgrid-scale models used in large-eddy simulations of the atmospheric boundary layer can reproduce their effect on the dynamics of the nonresolved scales. This ability is important especially when LES is used to study transport processes at the land–atmosphere interface. Eddy diffusivity models cannot reproduce backscatter of energy or scalar variance from the small to the resolved scales. Existing models that include backscatter effects in LES use stochastic forcing (e.g., Mason and Thomson 1992; Schumann 1995), while others are based on scale-similarity arguments (e.g., Bardina 1983; Liu et al. 1994). Being random and oblivious to details of stability, present stochastic models cannot reproduce the observed conditional statistics. On the other hand, similarity models may capture such effects. Further tests and field measurements to address these issues are left for future work.

Also, notice that current experiments (and those in Porté-Agel et al. 1998) do not include the dissipation based on the vertical component $\chi_3 = -q_3(\partial\tilde{\theta}'/\partial x_3)$. Data from further experiments that allow resolution of χ_3 will be the subject of future studies.

Acknowledgments. The authors gratefully acknowledge the field assistance of Li-Chuan Chen and Zhiming Chen and the cooperation of the administration and staff at the Amana Colonies. The authors also acknowledge funding from NSF-ATM-9726270 and the loan of equipment from Dr. Gabriel Katul of Duke University.

REFERENCES

Albertson, J. D., and M. B. Parlange, 1999a, Natural integration of scalar fluxes from complex terrain. *Adv. Water Res.,* **23,** 239–252.

——, and ——, 1999b: Surface length scales and shear stress: Implications for land–atmosphere interaction over complex terrain. *Water Resour. Res.,* **35,** 2121–2132.

Andrén, A., A. R. Brown, J. Graf, P. J. Mason, C.-H. Moeng, F. T. M. Nieuwstadt, and U. Schumann, 1994: Large-eddy simulation of the neutrally stratified boundary layer: A comparison of four computer codes. *Quart. J. Roy. Meteor. Soc.,* **120,** 1457–1484.

Avissar, R., and T. Schmidt, 1998: An evaluation of the scale at which ground-surface heat flux patchiness affects the convective boundary layer using large-eddy simulations. *J. Atmos. Sci.,* **55,** 2666–2689.

——, E. W. Eloranta, K. Gürer, and G. J. Tripoli, 1998: An evaluation of the large-eddy simulation option of the Regional Atmospheric Modeling System in simulating a convective boundary layer: A FIFE case study. *J. Atmos. Sci.,* **55,** 1109–1130.

Bardina, J., 1983: Improved turbulence models based on large eddy simulation of homogeneous, incompressible, turbulent flows. Ph.D. dissertation, Stanford University, 174 pp.

Clark, R. G., J. H. Ferziger, and W. Reynolds, 1979: Evaluation of subgrid models using an accurately simulated turbulent flow. *J. Fluid Mech.,* **91,** 1–16.

Domaradski, J. A., W. Liu, and M. E. Brachet, 1993: An analysis of

subgrid-scale interactions in numerically simulated isotropic turbulence. *Phys. Fluids A,* **5,** 1747–1759.

Dwyer, M. J., E. G. Patton, and R. H. Shaw, 1997: Turbulent kinetic energy budgets from a large-eddy simulation of airflow above and within a forest canopy. *Bound.-Layer Meteor.,* **84,** 23–43.

Gao, W., and R. H. Shaw, 1992: Conditional analysis of temperature and humidity microfronts and ejection/sweep motions within and above a deciduous forest. *Bound.-Layer Meteor.,* **59,** 35–57.

——, ——, and K. T. Paw U, 1989: Observation of organized structure in turbulent flow within and above a forest canopy. *Bound.-Layer Meteor.,* **47,** 349–377.

Härtel, C., and L. Kleiser, 1993: Energy transfer between large and small scales in wall-bounded turbulent flows. *Engineering Applications of Large Eddy Simulations,* U. Piomelli and S. Ragab, Eds., ASME.

Katul, G., C.-I. Hsieh, and J. Sigmon, 1997a: Energy–inertial scale interactions for velocity and temperature in the unstable atmospheric surface layer. *Bound.-Layer Meteor.,* **82,** 49–80.

——, G. Kuhn, J. Schieldge, and C.-I. Hsieh, 1997b: The ejection–sweep character of scalar fluxes in the unstable surface layer. *Bound.-Layer Meteor.,* **83,** 1–26.

Kiely, G., J. D. Albertson, M. B. Parlange, and W. E. Eichinger, 1996: Convective scaling of the average dissipation rate of temperature variance in the atmospheric surface layer. *Bound.-Layer Meteor.,* **77,** 267–284.

Lin, C.-L., 1999: Near-grid-scale energy transfer and coherent structures in the convective planetary boundary layer. *Phys. Fluids,* **11,** 3482–3494.

Liu, S., C. Meneveau, and J. Katz, 1994: On the properties of similarity subgrid-scale models as deduced from measurements in a turbulent jet. *J. Fluid Mech.,* **275,** 83–119.

Mason, P. J., 1994: Large-eddy simulation: A critical review of the technique. *Quart. J. Roy. Meteor. Soc.,* **120,** 1–26.

——, and D. J. Thomson, 1992: Stochastic backscatter in large-eddy simulations of boundary layers. *J. Fluid Mech.,* **242,** 51–78.

Meneveau, C., 1991: Analysis of turbulence in the orthonormal wavelet representation. *J. Fluid Mech.,* **232,** 469–520.

——, 1994: Statistics of turbulence subgrid-scale stresses: Necessary conditions and experimental tests. *Phys. Fluids,* **6,** 815–833.

Moeng, C.-H., 1984: A large-eddy-simulation model for the study of planetary boundary-layer turbulence. *J. Atmos. Sci.,* **41,** 2052–2062.

Nieuwstadt, F. T. M., P. J. Mason, C.-H. Moeng, and U. Schumann, 1991: Large-eddy simulation of the convective boundary layer: A comparison of four computer codes. *Turbulent Shear Flows,* **8,** 343–367.

O'Neil, J., and C. Meneveau, 1997: Subgrid-scale stresses and their modeling in a turbulent plane wake. *J. Fluid Mech.,* **349,** 253–293.

Parlange, M. B., W. E. Eichinger, and J. D. Albertson, 1995: Regional scale evaporation and the atmospheric boundary layer. *Rev. Geophys.,* **33** (1), 99–124.

Peltier, L. J., J. C. Wyngaard, S. Khanna, and J. G. Brasseur, 1996: Spectra in the unstable surface layer. *J. Atmos. Sci.,* **53,** 49–61.

Piomelli, U., P. Moin, and J. H. Ferziger, 1988: Model consistency in large eddy simulation of turbulent channel flows. *Phys. Fluids,* **31,** 1884–1891.

——, Y. Yu, and R. J. Adrian, 1996: Subgrid-scale energy transfer and near-wall turbulence structure. *Phys. Fluids,* **8,** 215–224.

Porté-Agel, F., C. Meneveau, and M. B. Parlange, 1998: Some basic properties of the surrogate subgrid-scale heat flux in the atmospheric boundary layer. *Bound.-Layer Meteor.,* **88,** 425–444.

Press, W. C., S. A. Teukolsky, W. T. Vetterling, and B. P. Flannery, 1992: *Numerical Recipes.* Cambridge University Press, 963 pp.

Raupach, M. R., R. A. Antonia, and S. Rajagopalan, 1991: Rough-wall turbulent boundary layers. *Appl. Mech. Rev.,* **44,** 1–25.

Schumann, U., 1995: Stochastic backscatter of turbulence energy and scalar variance by random subgrid-scale fluxes. *Proc. Roy. Soc. London A,* **451,** 293–318.

Shaw, R. H., and U. Schumann, 1992: Large-eddy simulation of turbulent flow above and within a forest. *Bound.-Layer Meteor.,* **61,** 47–64.

——, J. Tavangar, and D. Ward, 1983: Structure of the Reynolds stress in a canopy layer. *J. Climate Appl. Meteor.,* **22,** 1922–1931.

——, K. T. Paw U, and W. Gao, 1989: Detection of temperature ramps and flow structures at a deciduous forest site. *Agric. For. Meteor.,* **47,** 123–138.

Sorbjan, Z., 1996: Effects caused by varying strength of the capping inversion based on a large-eddy simulation of the shear-free convective boundary layer. *J. Atmos. Sci.,* **53,** 2015–2024.

Sullivan, P. P., J. C. McWilliams, and C.-H. Moeng, 1994: A subgrid-scale model for large-eddy simulation of planetary boundary-layer flows. *Bound.-Layer Meteor.,* **71,** 247–276.

Szilagyi, J., M. B. Parlange, G. G. Katul, and J. D. Albertson, 1999: An objective method for determining principal time scales of coherent eddy structures using orthonormal wavelets. *Adv. Water Res.,* **22,** 561–566.

Tong, C., J. C. Wyngaard, S. Khanna, and J. G. Brasseur, 1998: Resolvable- and subgrid-scale measurement in the atmospheric surface layer: Technique and issues. *J. Atmos. Sci.,* **55,** 3114–3126.

Wyngaard, J. C., and S. F. Clifford, 1977: Taylor's hypothesis and high-frequency turbulence spectra. *J. Atmos. Sci.,* **34,** 922–929.